Geomechanics and Engineering, *Vol. 25, No. 1 (2021) 59-73*
DOI: https://doi.org/10.12989/gae.2021.25.1.059

Evaluation of geological conditions and clogging of tunneling using machine learning

Xue-Dong Bai[1,2a], Wen-Chieh Cheng*[1], Dominic E.L. Ong[3b] and Ge Li[1,2c]

[1]*School of Civil Engineering, Xi'an University of Architecture and Technology, Xi'an 710055, China*
[2]*Shaanxi Key Laboratory of Geotechnical and Underground Space Engineering (XAUAT), Xi'an 710055, China*
[3]*School of Engineering and Built Environment, Griffith University, Queensland 4111, Australia*

(Received October 25, 2020, Revised March 7, 2021, Accepted March 9, 2021)

Abstract. There frequently exists inadequacy regarding the number of boreholes installed along tunnel alignment. While geophysical imaging techniques are available for pre-tunnelling geological characterization, they aim to detect specific object (e.g., water body and karst cave). There remains great motivation for the industry to develop a real-time identification technology relating complex geological conditions with the existing tunnelling parameters. This study explores the potential for the use of machine learning-based data driven approaches to identify the change in geology during tunnel excavation. Further, the feasibility for machine learning-based anomaly detection approaches to detect the development of clayey clogging is also assessed. The results of an application of the machine learning-based approaches to Xi'an Metro line 4 are presented in this paper where two tunnels buried in the water-rich sandy soils at depths of 12-14 m are excavated using a 6.288 m diameter EPB shield machine. A reasonable agreement with the measurements verifies their applicability towards widening the application horizon of machine learning-based approaches.

Keywords: Xi'an Metro; EPB shield; machine learning; clogging; silt soil

1. Introduction

In recent years, shield tunnelling method has been widely adopted for tunnel excavation in densely populated urban areas and is considered as a popular alternative to open-cut construction because of its efficient construction and reduced environmental impact (Javadi and Rezania 2009, Zhang *et al.* 2016, Xu *et al.* 2017, Gao *et al.* 2017, Wang *et al.* 2018, Luat *et al.* 2020b, Liu *et al.* 2020). However, shield tunnelling in a heterogeneous ground that often confronts in practice can easily trigger geo-hazard such as water ingress and subsequently surface subsidence (Goh and Hefney 2010, Mazek 2014, Lee *et al.* 2016, Eskandari *et al.* 2018, Rezaei *et al.* 2019). Inappropriate tunnelling parameters (e.g., thrust force, face pressure, advance rate, cutterwheel rotational speed and rate of spoil removal) may aggravate the geo-hazard a step further (Cheng *et al.* 2017, 2019a). Further, a small number of geological boreholes installed along tunnel alignment may not be able to provide details regarding strata sequence, distribution of alternating layers, location of karst cavern and so on despite some alternative available (Cheng *et al.* 2018).

While geophysical imaging techniques exist for pre-tunnelling geological characterization (Li *et al.* 2015, Sheil *et al.* 2016, Liu *et al.* 2017a, b, Li *et al.* 2018a, b, O'Dwyer *et al.* 2019, Cheng *et al.* 2019b, 2020a, c), they are designed for detecting water body and/or karst cave underground. Therefore, there remains significant motivation in the industry to develop a real-time identification technology relating complex geological conditions with the tunnelling parameters (Cheng *et al.* 2020b).

Further, the cutterwheel, while tunnelling in clayey soils, is pressed into the tunnel face and the plastically deformable soil is pushed to both sides in the form of 'lumps'. Free water (e.g., groundwater) can transform the consistency of the cut lumps into a sticky consistency. In this context, uncritical soils turn into sticky material towards clogging the excavation at the tunnel face (Fountaine 1954). The clogging, however, happens throughout process from the excavation at the tunnel face (i.e., primary clogging) up to separation and disposal (i.e., secondary clogging) and can cause unplanned downtimes. Therefore, a pre-assessment for the development of clogging is deemed necessary prior to tunnel excavation. An increasing popular means of assessing the development of clogging is through a combination of the plasticity index $I_p = \omega_L - \omega_P$ and the consistency index $I_c = (\omega_L - \omega_n)/(\omega_L - \omega_P)$. According to Thewes (1999), clayey soils with $I_p > 20\%$ and $I_c = 0.75$-1.25 have the highest potential to lead to clogging. However, more recent studies have shown that extensive clogging can even occur in clayey soils with $I_c = 1.25$-1.50 (Thewes 1999). Hollmann and Thewes (2013)

*Corresponding author, Professor
E-mail: w-c.cheng@xauat.edu.cn
[a]Ph.D. Student
E-mail: baixuedong@xauat.edu.cn
[b]Senior Lecturer
E-mail: d.ong@griffith.edu.au
[c]Ph.D. Student
E-mail: lige@xauat.edu.cn

ISSN: 2005-307X (Print), 2092-6219 (Online)

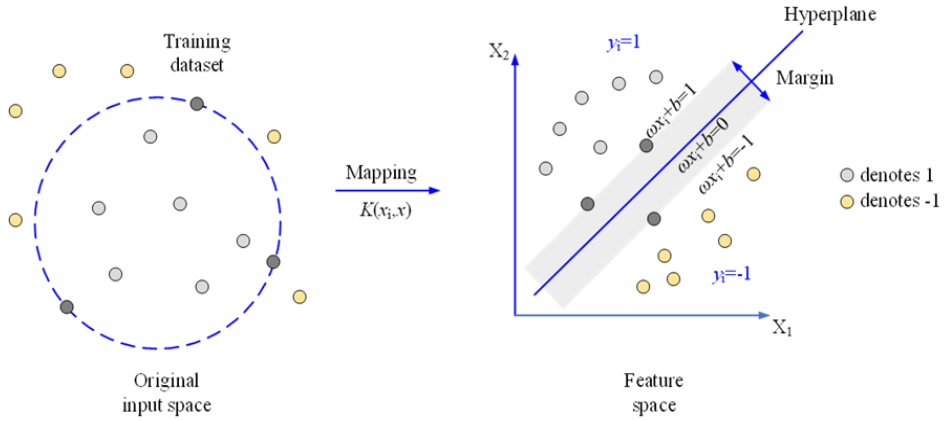

Fig. 1 Transformation of original input space into feature space and hyperplane construction

examined 150 samples of 'sticky' material from open and slurry-supported shield tunnelling projects. The samples varied between very soft (23% of samples; I_c = 0.4-0.5), soft-medium (58%; I_c = 0.5-0.75) and stiff (19%; I_c = 0.75-1.0) consistency. Laboratory test results from Feinendegen *et al.* (2011) are in line with those reported by Hollmann and Thewes (2013). Shield tunnelling in clayey soils with 'soft' consistency is, therefore, considered high-risk for the development of clogging (Spagnoli *et al.* 2011a, b, Thewes and Hollmann 2014, 2016, Basmenj *et al.* 2016, Park *et al.* 2018).

Tunnelling data that closely relate to surrounding geology have largely proliferated by modern tunnel boring machines (TBMs) in recent years and present a substantial opportunity for the application of data-driven approaches that possess an ability to infer patterns from data without reference to known, or labelled, outcomes. In other words, we treat modern TBMs as a 'sensor' underground to sense, in this case, the change in geology and the development of clogging. The objectives of this paper are: (1) to characterise the response of tunnelling parameters to the change in geology and the development of clogging, (2) to assess the feasibility for the use of machine learning (ML)-based data-driven approaches to identify geological conditions and (3) to evaluate the development of clogging through a combination of the ML-based anomaly detector and the semi-empirical approach.

2. Classification and anomaly detection

2.1 Numerical simulation procedure

Identifying characteristics of the measured system by using information retrieved from the measured data rather than modelling the system response is the 'know-how' of machine learning approaches. The aim of this work is to develop an improved understanding regarding the relation of the existing tunnelling parameters with known geological conditions during tunnel excavation, in which case 'supervised' machine learning is the optimal problem-solving tool. Multivariate Adaptive Regression Splines (MARS), Random Forest (RF) and Support Vector Machines (SVMs) are popular supervised machine learning algorithms. MARS is a nonparametric statistical method based upon a 'divide and conquer' strategy (Friedman 1991, Zhang *et al.* 2018, Luat *et al.* 2020a). While MARS generates a model capable of handling both linear and nonlinear relationships, its drawback corresponds to low accuracy for sparse data.

RF is a 'tree-based' method where each tree learns from its predecessors and updates the residue errors successively ensuring the trees always learn an updated version of the residues when they grow subsequently in the order (Breiman 2001).

However, RF is deemed susceptible to overfitting when subjected to small datasets. In light of these limitations, SVM is chosen because of its ability to resist the influence arising by the number of inputs, meaning that it is well conditioned for high-dimensional datasets. Further, the use of kernels captures complex input-output mapping.

SVMs (termed 'SVM classifier' hereafter) can lift data that cannot be separated using a straight line to a space with a high dimension where a straight hyperplane can separate the data into different classes using linear or non-linear kernels (see Fig. 1). The hyperplane forms a non-linear curve when mapping back to the original input space. The hyperplane is represented by Eq. (1).

$$\begin{aligned} \boldsymbol{w}\cdot x_i + b \geq 1 \quad & if \;\; y_i = 1 \\ \boldsymbol{w}\cdot x_i + b \leq -1 \quad & if \;\; y_i = -1 \end{aligned} \tag{1}$$

where $\boldsymbol{w}$ = adaptive weight vector, x = input vector, y_i = associated labels and b = bias. The hyperplane searches for the maximum margin between classes. The larger the margin, the clearer the decision boundary and the better the classifier performance. The objective function of the SVM classifier is:

$$\begin{aligned} & \frac{1}{2}||w||^2 + C\sum_{i=1}^{n}\xi_i, \quad i = 1,2,\dots,n \\ & y_i(w^T\cdot x_i + b) \geq 1 - \xi_i \\ & \xi_i \geq 0, \quad i = 1,2,\dots,n \end{aligned} \tag{2}$$

where C = non-negative penalty constant, n = number of observation and ξi = slack variable in Eq. (2). The decision

function for a data point x becomes Eq. (3) when this minimisation problem is solved by means of Lagrange multipliers.

$$f(x) = \sum_{i=1}^{n} y_i \alpha_i K(x_i, x_j) + b \quad (3)$$

where α = Lagrange multiplier. As the outcome of the decision function only relies upon the dot-product of the vectors in the feature space, there is no necessity to conduct an explicit mapping to that space. Provided a kernel function K generates the same results, it can be used instead. The Radial basis function (RBF) which is arguably the most common kernel function is used here in Eq. (4):

$$K(x_i, x_j) = exp\left(-\frac{\|x_i - x_j\|^2}{2\gamma^2}\right) \quad (4)$$

where γ = kernel parameter varying from 0 to 1 and $||x_i - x_j||$ is the dissimilarity measure.

2.2 Anomaly detection

Many machine learning algorithms attempt to deal with the two or multi-class situation. Schölkopf *et al.* (2001) framed the One-class SVM (OCSVM) approach by taking into account the origin as the only member of the second class. Therefore, a hyperplane, constructed in the feature space, aims to separate the dataset from the origin through a maximum margin. Here the OCSVM (termed 'OCSVM detector' hereafter) is to detect the development of clogging using a combination of the existing tunnelling parameters and the semi-empirical approach. The objective function and the decision function for the OCSVM detector are similar to those applied to the SVM classifier and their mathematical formulae are, therefore, neglected to avoid repetition. Kernel functions have been introduced for sequence data, graphs, text, images, as well as vectors. This approach is called the 'kernel trick' which allows the dot-product to be substituted by kernel functions. Popular kernels that are used in various kernelised learning algorithms are Fisher kernel, Polynomial kernel, Radial basis function (RBF) kernel and Neural network Gaussian process (NNGP) kernel. Since the value of the RBF kernel decreases with increase of distance and ranges between 0 (within the limit) and 1 (when $x_i = x_j$), it has a ready interpretation as a similarity measure. Further, the feature space of the RBF kernel is capable of extending to an infinite number of dimensions. The RBF kernel is, therefore, selected here (Sheil *et al.* 2020).

2.3 Feature selection

A typical thrust force-distance plot is non-stationary, which causes some difficulty in direct application of SVMs. Further, the use of stationary data is desirable to accentuate patterns in the data. To this end, decomposition procedures can be introduced to disaggregate time series data into feature-based sub-series. Decomposition techniques are to isolate salient features of a dataset (Persons 1919). One of the most popular decomposition techniques is seasonal-

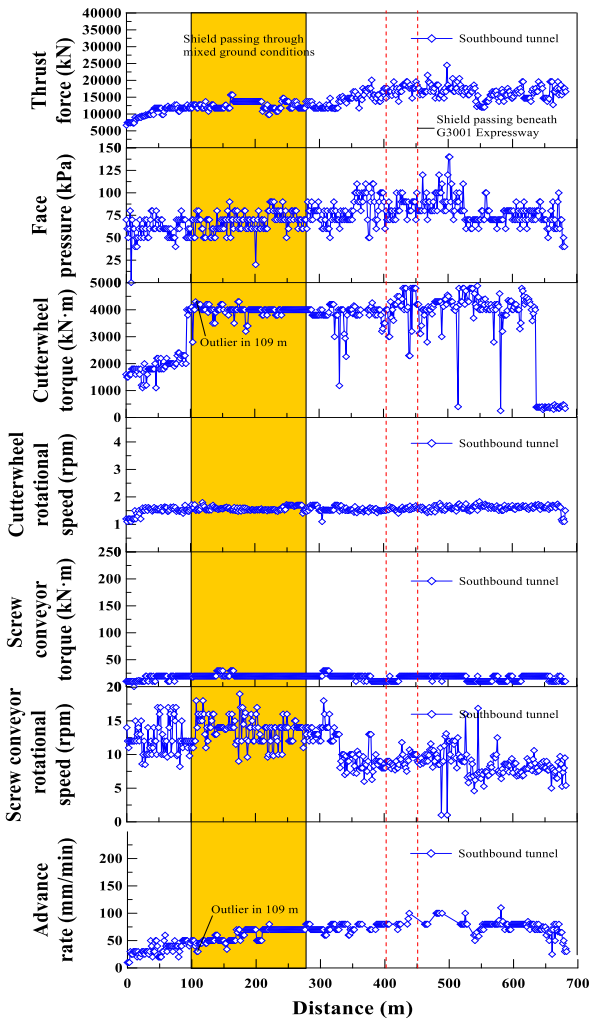

Fig. 2 EPB shield tunnelling activities for the southbound tunnel

trend decomposition using Loess smoothing (STL; Cleveland *et al.* 1990) which partitions the global series into three additive components in Eq. (5):

$$y_t = P_t + T_t + R_t \quad (5)$$

where P_t = periodic component, T_t = trend component and R_t = residue component. In this work, no significant periodic component was identified. Two feature variables are considered for the application of SVMs, namely the trend and residual components (i.e., T_t and R_t). In time series decomposition, the periodic component is used to set the length of the period to smooth the initial data. The trend component and the residual component respectively represent the overall development trend of the data and the degree of deviation of a single data, which makes it easier to highlight the characteristics of the data patterns. Since the thrust force, the cutterwheel torque, the advance rate and the screw conveyor rotational speed from tunnelling in the gravelly, coarse and medium sands present a pattern distinguishable from tunnelling in the fine sand (see Figs. 2 and 3), the four tunnelling parameters are decomposed into the trend and residual components for the classification analysis. Further, as the shear strength of the sticky material

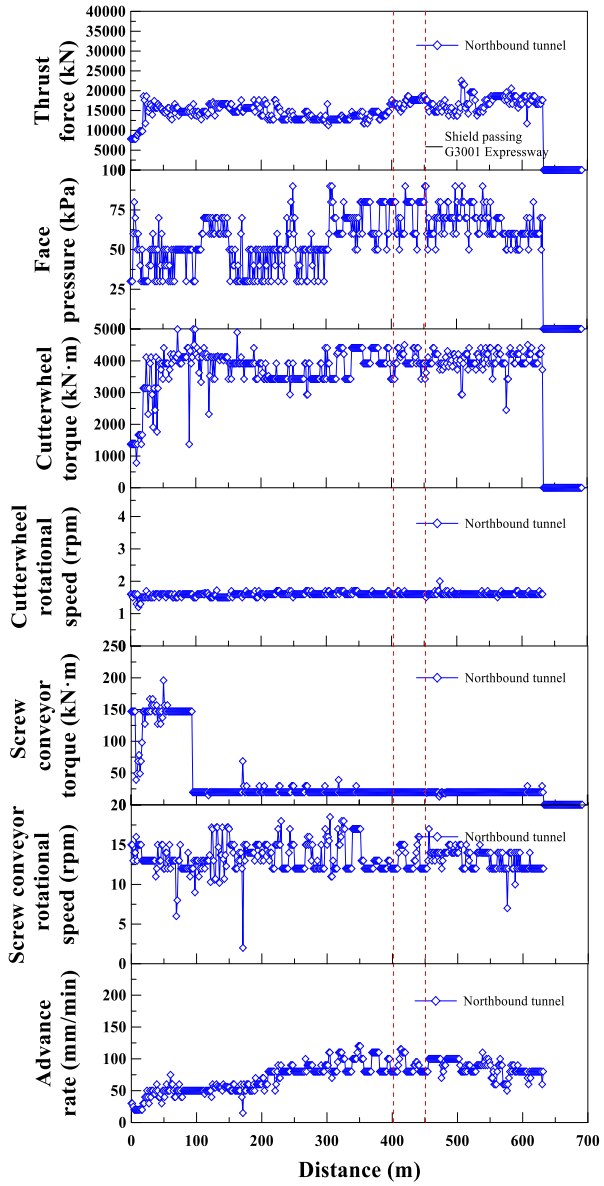

Fig. 3 EPB shield tunnelling activities for the northbound tunnel

is capable of withstanding the mechanical forces exerted while scraping soils at the face and slow the advance rate, two out of the four parameters, namely the cutterwheel torque and the advance rate, are deemed sensitive to the development of clogging and decomposed into the trend and residual components.

2.4 Optimisation of hyperparameters

Grid search (GS) aims to perform an exhaustive search on a defined subset of the hyperparameter space (Xu *et al.* 2019). The hyperparameters are defined using 'lower bound', 'upper bound' and 'number of steps'. The data is split into k subsets and the value of k is generally set to 10 in most cases. After trials against various combinations of hyperparameters, the one with the highest cross-validation accuracy is selected to train a GS-SVM model on the whole dataset. The main steps of the process are detailed as follows (see Fig. 4):

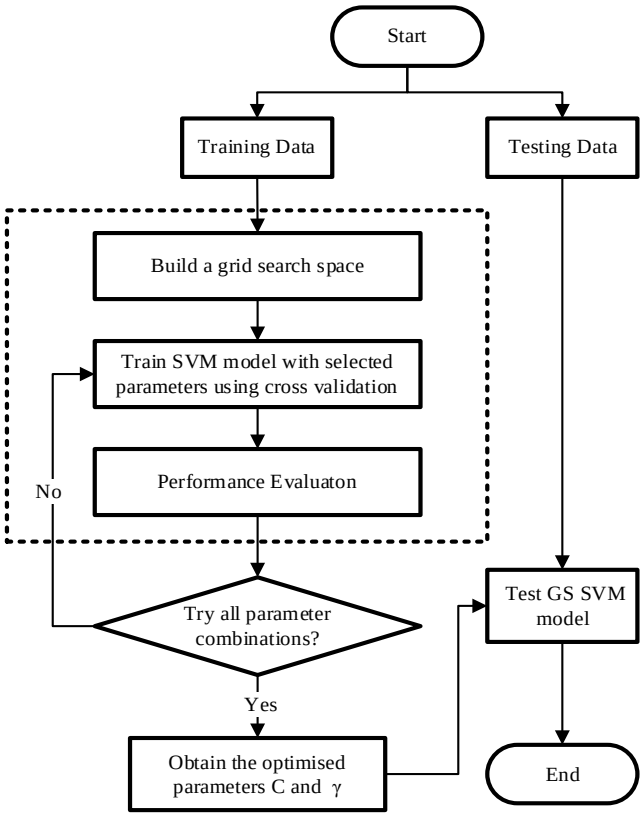

Fig. 4 Flowchart of the GS-SVM algorithm

Table 1 EPB shield machinery parameters

	EPB shield (Lovat)
Excavation diameter (mm)	6,288
External diameter (mm)	6,000
Internal diameter (mm)	5,400
Shield length (incl. cutterwheel) (mm)	9,070
Liner thickness (mm)	300
Liner length (mm)	1,500
Cutterwheel rotational speed (rpm)	0-3.5
Total installed power (kW)	1,450
Face pressure (kPa)	500
Cutterwheel opening ratio (%)	44
Maximum torque (kN·m)	6,620
Maximum thrust force (kN)	36,000

Step 1: Construct a grid search space.

Step 2: Train the SVM model with various combinations of hyperparameters by a cross-validation technique.

Step 3: Evaluate the performance of GS-SVM model.

Step 4: Terminate the process once all the combinations of hyperparameters have been tried.

Step 5: Determine the optimised hyperparameters and

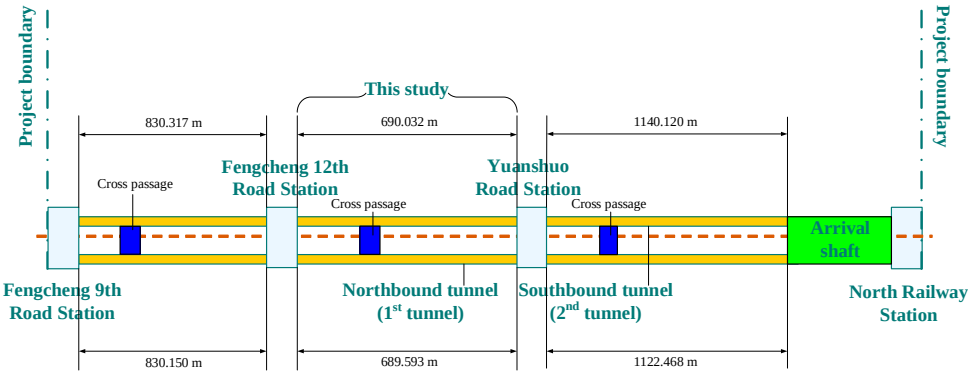

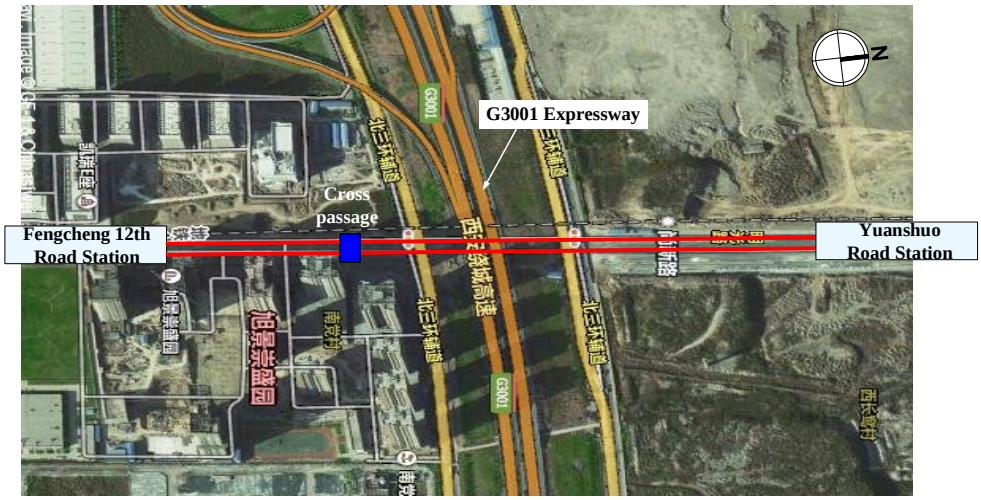

Fig. 5 Project layout and study area for Xi'an Metro line 4

Table 2 Subsoil properties

Layer	γ (kN/m^3)	γ_d (kN/m^3)	ω (%)	ω_L (%)	ω_P (%)	e (-)	G_s	c' (kN/m^2)	ϕ' (deg.)	SPT-N	E_s (kN/m^2)
Surface backfill	11.5	13.5	20	-	-	1.05	-	5	8	-	-
Coarse sand	19.8	16.5	19.8	-	-	0.62	2.67	0	35	-	17
Median sand	19.8	16.4	20.4	-	-	0.63	2.67	0	32.5	40	13
Silty clay	19.9	16	24.6	33.6	19.8	0.70	2.72	23	0	26	7

Note: γ=bulk unit weight; γ_d=dry unit weight; ω=moisture content; ω_L=liquid limit; ω_P=Plastic limit;e=void ratio; G_s=specific gravity; c'=cohesion; ϕ'=friction angle; SPT-N=blow count value; E_s=Young's ground modulus

re-train the GS-SVM model with the optimised hyperparameters.

2.5 Confusion matrix

Four outcomes can be summarised in a 'confusion matrix', namely (a) true positive (TP), (b) false negative (FN), (c) false positive (FP) and (d) true negative (TN). In this work, 'TP' denotes a geological condition of fine sand which has been correctly classed, while 'FN' indicates that the fine sand has been erroneously classed as the coarse sand. The discovery rate (DR) and the false alarm rate (FAR) are calculated based upon the four outcomes, thereby evaluating the performance of the GS-SVM model.

3. Case History: Xi'an Metro line 4

3.1 Project overview

The project present in this study belongs to a part of Xi'an Metro line 4. There are six tunnels built using the shield tunnelling method, with three cross passages, and they are responsible for joining four stations with each other, namely Fengcheng 9th Road Station, Fengcheng 12th Road Station, Yuanshuo Road Station and North Railway Station. Fig. 5 depicts the project layout. The length of each tunnel varies from 689.6 m to 1140.1 m. This study mainly focuses on the two tunnels between the Fengcheng 12th Road Station and the Yuanshuo Road Station. The milage

Table 3 EPB shield initial tunnelling parameters

	EPB shield (Lovat)
Thrust force (kN)	12,000-17,000
Cutterwheel torque (kN·m)	4,500-5,500
Cutterwheel rotational speed (rpm)	1-2
Advance rate (mm/min)	20-35
Face pressure (kPa)	40
Volume of bentonite injected (m^3/ring)	5-6
Volume of foam injected (litre/ring)	80-100
Rate of spoil removal (m^3/ring)	51-55

Table 4 EPB shield modified tunnelling parameters

	EPB shield (Lovat)
Thrust force (kN)	12,000-17,000
Cutterwheel torque (kN·m)	3500-4500
Cutterwheel rotational speed (rpm)	1-2
Advance rate (mm/min)	40-60
Face pressure (kPa)	60
Volume of bentonite injected (m^3/ring)	5
Volume of foam injected (litre/ring)	63
Tunnelling spoil disposal (m^3)	52

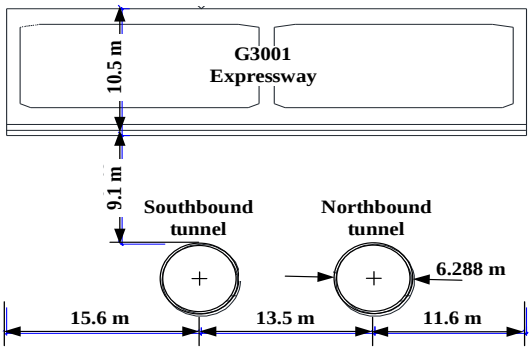

Fig. 6 Illustration of relative position between G3001 Expressway and the shield tunnels

for the northbound tunnel is 689.593 m, while for the southbound tunnel it is 690.032 m. A 6.288 m diameter EPB shield machine advanced in the water-rich sandy soils at depths of 12-14 m. In the study area, the EPB shield machine passed underneath a culvert of G3001 Expressway (see Fig. 6). The shield machinery parameters are tabulated in Table 1, while the subsoil properties are shown in Table 2. When the machine passes beneath the G3001 highway, the development of surface settlement and adverse impact on the culvert show a great necessity of modifying the tunnelling parameters towards preventing settlement in

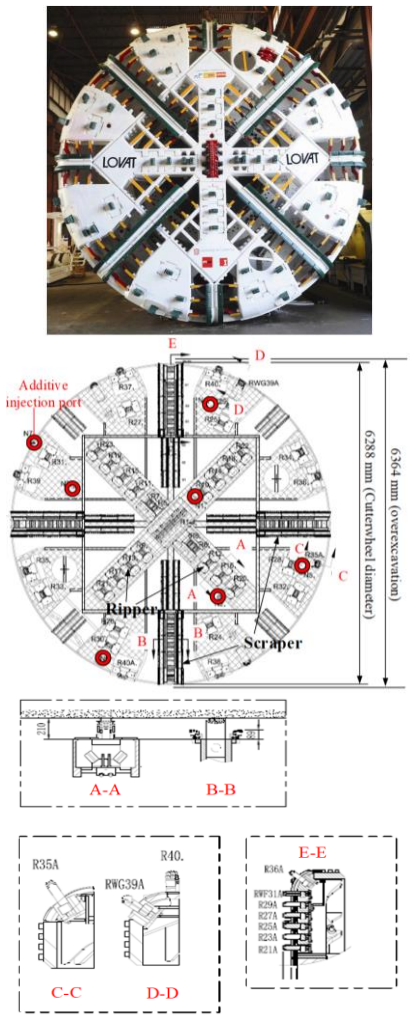

Fig. 7 EPB shield machine cutterwheel configuration and cutter details Expressway and the shield tunnels

excess of the designed limit and damage to the culvert from occurring. The most significant modification refers to the cutterwheel torque, advance rate, and face pressure (see Tables 3 and 4). The range of cutterwheel torque changes from 4500-5500 kN·m to 3500-4500 kN·m. Further, the range of advance rate is lifted from 20-35 mm/min up to 40-60 mm/min, while the face pressure changes from 40 kPa to 60 kPa. The greater face pressure aims to manage the development of surface settlement. The faster the advance rate, the smaller the disturb to surrounding environment. It is worth noting that the excavation performance remains nearly the same despite a little decline in the cutterwheel torque. The cutterwheel configuration and cutter details are depicted in Fig. 7. Tunnel lining with continuous segmental rings is usually designed against external earth pressures. In this project, a typical segmental ring is 6 m in diameter and composed of six segments of 0.3 m in thickness towards creating about 30 cm annular gap. The annular gap is filled with grouts using the synchronous grouting when the segmental ring has erected and left the EPB shield tail (Table 5). The secondary grouting is conducted to fill cavities likely to be left after the shrinkage of injected grouts from the synchronous grouting.

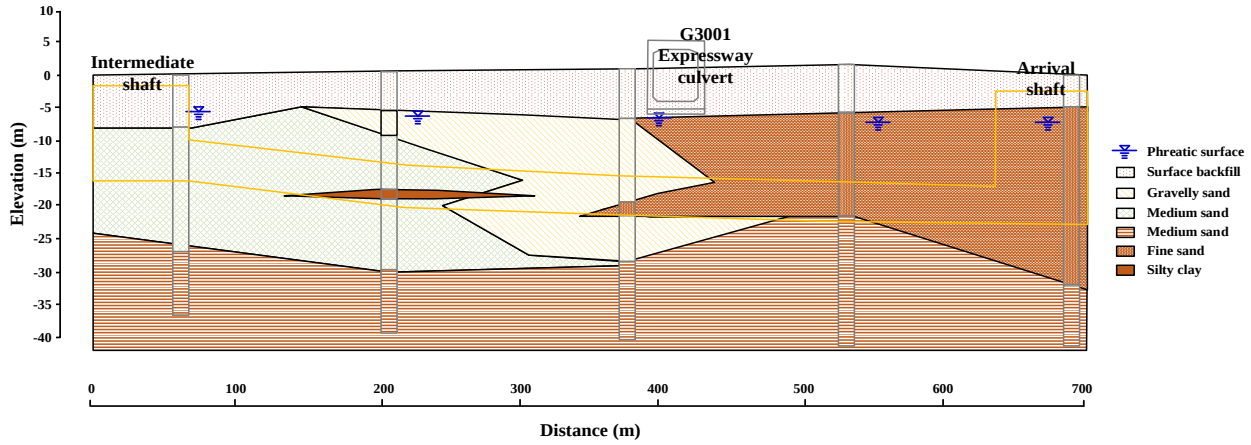

(a) Southbound tunnel

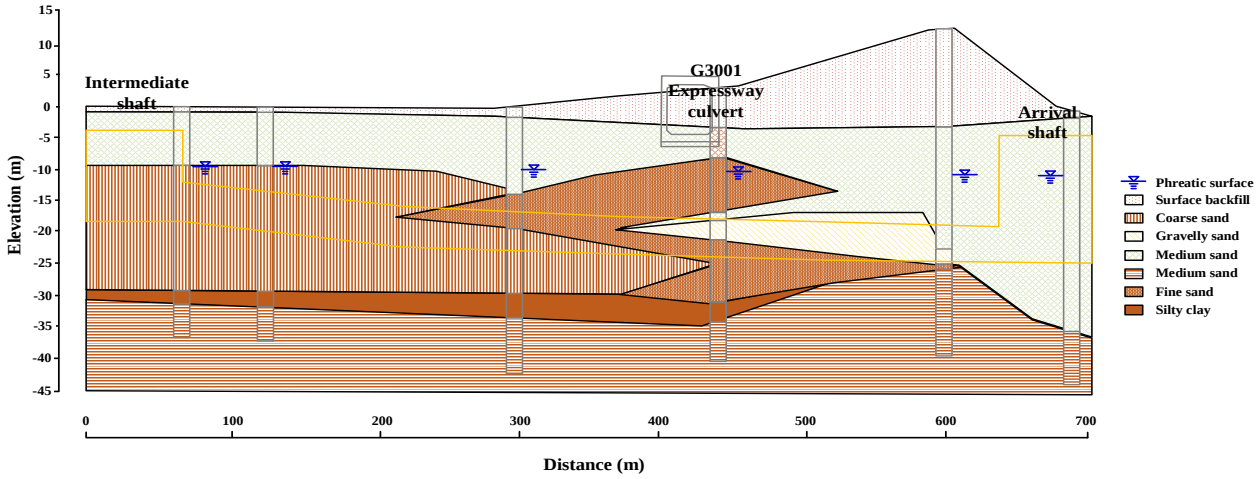

(b) Northbound tunnel

Fig. 8 Geological profile along tunnel alignment

Table 5 Synchronous and secondary grout mixes

(a) Synchronous grouting	Parameters
Cement	185 kg
Coal ash	230 kg
Bentonite	60 kg
Sand	860 kg
Water	400 kg
Gel time	4 hours
(b) Secondary grouting	Parameters
Cement slurry (grout A)	1:1.3 (cement:water)
Sodium silicate (grout B)	1:1 (sodium silicate:water)
Gel time	35 secs

Note: for grout A the ratio of cement to water is measured by weight, while for grout B the ratio of sodium silicate to water is measured by volume

3.2 Engineering geology

Fig. 8 summarises the ground conditions as determined from 11 boreholes positioned close to the tunnel alignments.

The ground is composed of surface backfill, medium sand, occasional interbedded silty clay, gravelly sand and fine sand. The moisture content ω, void ratio e and specific gravity G_s for the coarse sand, the median sand and silty clay are in ranges of 19.8-24.6%, 0.62-0.70 and 2.67-2.72 respectively. The liquid limit ω_L for the silty clay is tested as 33.6%. The permeability for the sandy soils is measured as high as 3×10^{-2} cm/s. The phreatic surface is at 6 m depth below the ground surface. Apart from that, the direct shear (DS) test results show that the friction angle for the coarse sand, medium sand and fine sand is 35°, 32.5° and 31.5° respectively, whereas the cohesion for the silty clay is 23 kPa according to the unconsolidated undrained (UU) test results (Table 2).

4. Results and discussion

4.1 Results

Optimising the hyperparameters is to obtain their combination which has the highest classification accuracy. The accuracy for each combination is summarised in Table 6, which is defined as the proportion of all correctly classified data (the sum of TPs and TNs) to all the data (the sum of TPs, TNs, FPs and FNs).

Table 6 Results of the machine learning-based approach

Tunnel	Parameters	Number of data	Hyperparameter C	Hyperparameter γ	TN	TP	FN	FP	Cross-validation accuracy
Southbound tunnel (2nd tunnel)	Thrust force	424	0.1668	2.1544	233	147	27	15	0.90
	Cutterwheel torque	424	0.60	27.8256	220	112	62	28	0.77
	Advance rate	424	7.7426	0.6	222	144	30	26	0.87
	Screw conveyor rotational speed	424	0.1668	0.6	213	157	17	35	0.88
Northbound tunnel (1st tunnel)	Thrust force	421	0.001	0.001	279	0	140	0	0.67
	Cutterwheel torque	421	0.6	100	270	85	55	9	0.71
	Advance rate	421	0.6	100	255	79	61	24	0.81
	Screw conveyor rotational speed	421	100	2.1544	276	12	128	3	0.69

Note: TP=true positive; TN=true negative; FP=false positive; FN=false negative

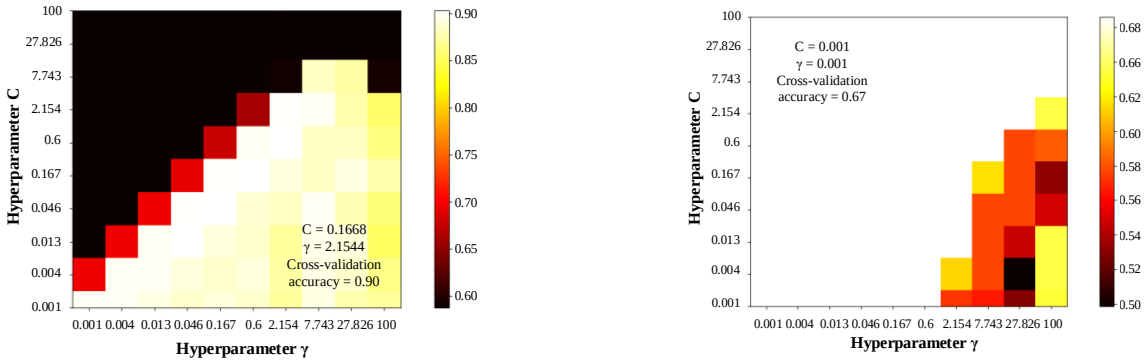

(a) The southbound tunnel (b) The northbound tunnel

Fig. 9 Contour of the cross-validation accuracy of the thrust force classifier

Fig. 9 shows the associated contours of the cross-validation accuracy. It can be seen that the contour presents in a symmetrical pattern when the cross-validation accuracy is approximately or higher than 80%. Most of the contours from the northbound tunnel are not in a symmetrical pattern, indicating that the cross-validation accuracy is lower compared with the southbound tunnel. The cross-validation accuracy for the southbound tunnel is measured up to 90%, while for the northbound tunnel it is as low as 67%. The classification results present hereafter correspond to the best hyperparameter combination.

Fig. 10 shows the performance of the GS-SVM model applied to the southbound tunnel mapped to the transformed space. Most of the coarse sands are correctly classed using the thrust force classifier, with FP = 15 (the lowest), whereas a majority of the fine sands are also correctly classed, with FN = 27.

The number of misclassifications = 42 (i.e., FN + FP) is the lowest amongst the four classifiers, with the highest cross-validation accuracy = 90%. The cutterwheel torque classifier correctly classes only two-third of the fine sands, with FN = 62. The same classifier induces FP = 28 towards causing the highest number of misclassifications = 90. The cross-validation accuracy associated with this case is the lowest, namely 77%. These results also indicate that a majority of FPs occur at 330-337 m distance, whereas most of FNs present at distances of 376-405 m and 530-630 m. It is noteworthy that most of the fine sands are correctly classed by the screw conveyor rotational speed classifier, with FN = 17 (the lowest). Fig. 11 presents the performance of the GS-SVM model applied to the northbound tunnel mapped to the feature space. It can be seen that most of the coarse sands are correctly identified by the cutterwheel torque classifier, with FP = 9.

Despite the lowest number of misclassifications = 64, the cross-validation accuracy = 71% is not the highest amongst the classifiers. The advance rate classifier causes the number of misclassifications higher than 64, with the highest cross-validation accuracy = 81% towards meaning that a low number of misclassifications do not correspond to high cross-validation accuracy. The cross-validation accuracy represents the performance of the GS-SVM model applied to the validation dataset rather than the performance applied to the whole dataset. It can also be seen that the thrust force classifier erroneously classes all of the fine sands as the coarse sands, with FN = 140. These results also indicate that FPs present at distances of 265-276 m and 531-567 m respectively, whereas FNs occur at 292-453 m

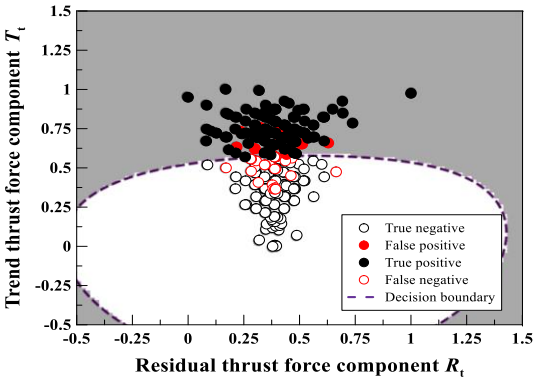

(a) Thrust force classifier

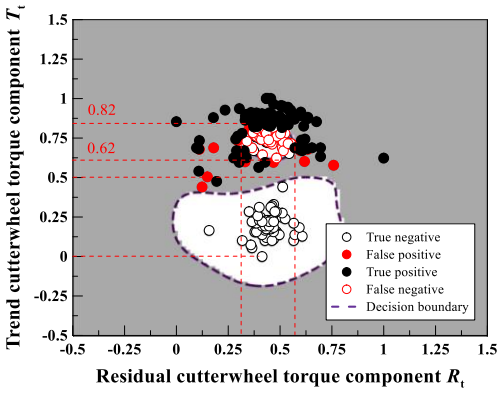

(b) Cutterwheel torque classifier

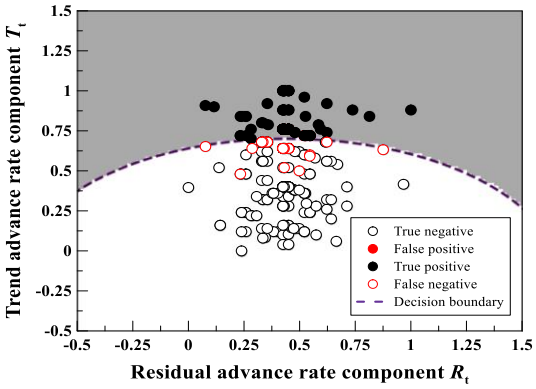

(c) Advance rate classifier

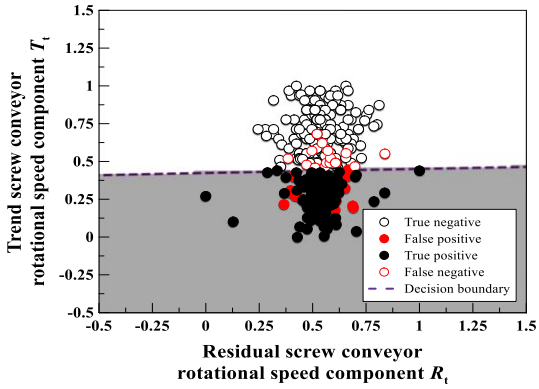

(d) Screw conveyor rotational speed classifier

Fig. 10 Performance of the GS-SVM model applied to the southbound tunnel mapped to transformed space

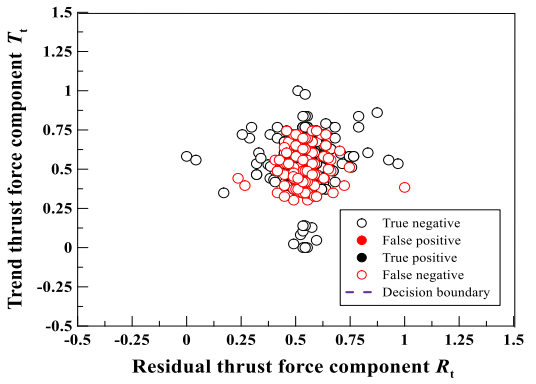

(a) Thrust force classifier

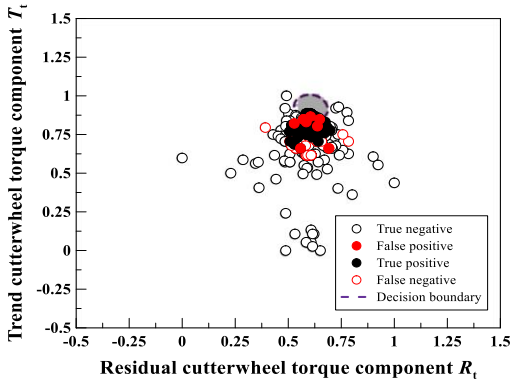

(b) Cutterwheel torque classifier

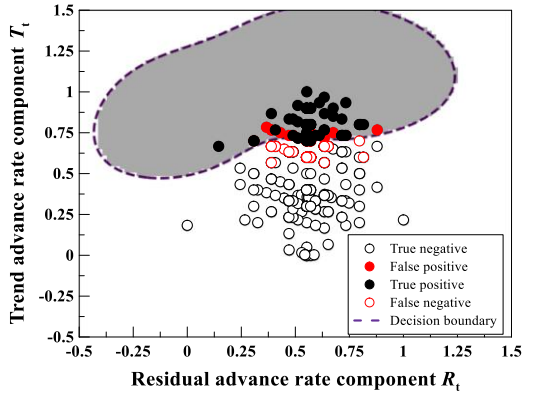

(c) Advance rate classifier

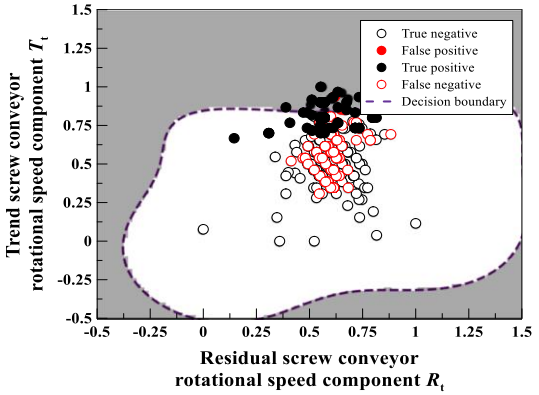

(d) Screw conveyor rotational speed classifier

Fig. 11 Performance of the GS-SVM model applied to the northbound tunnel mapped to transformed space

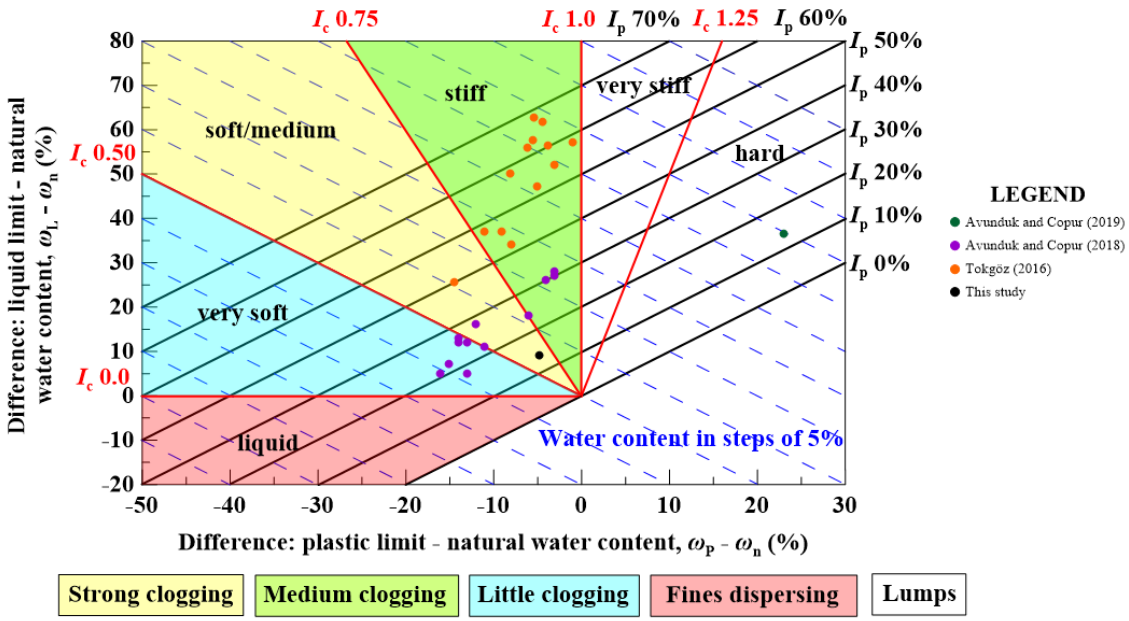

Fig. 12 Results of the semi-empirical approach applied to the southbound tunnel for detecting the clayey clogging

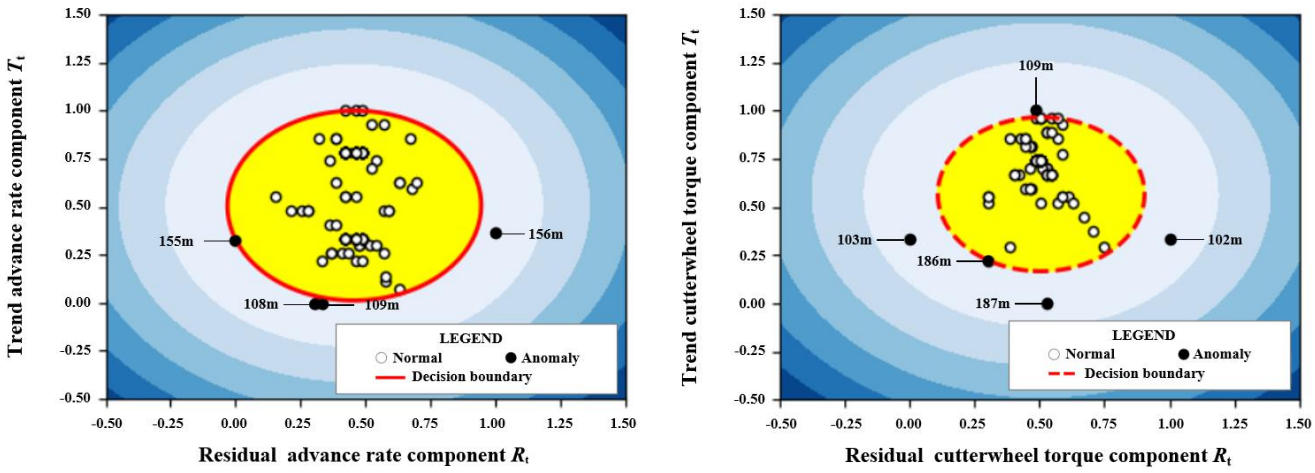

(a) Advance rate detector (b) Cutterwheel torque detector

Fig. 13 Performance of the anomaly detection approach applied to the southbound tunnel mapped to transformed space

Table 7 Performance of the machine learning-based approach

Tunnel	Parameters	Coarse sand identification		Fine sand identification	
		DR (%)	FAR (%)	DR (%)	FAR (%)
Southbound tunnel (2nd tunnel)	Thrust force	93.9	15.5	84.5	6.1
	Cutterwheel torque	88.7	35.6	64.4	11.3
	Advance rate	89.5	17.2	82.8	10.5
	Screw conveyor rotational speed	85.9	9.8	90.2	14.1
Northbound tunnel (1st tunnel)	Thrust force	100	100	0	0
	Cutterwheel torque	96.8	39.3	60.7	3.2
	Advance rate	91.4	43.6	56.4	8.6
	Screw conveyor rotational speed	98.9	91.4	8.6	1.1

Note: DR=TP/(TP+FN); FAR=FP/(FP+TN).

distance. On the whole, the constructed decision boundaries are clearer for the southbound tunnel than the northbound tunnel.

The semi-empirical approach is to assess the development of clogging during tunnel excavation and the results are regarded as the 'baseline'. Results from the ML-based anomaly detector are compared to the baseline assessment of clogging towards exploring the potential for the use of ML-based anomaly detectors for assessing the development of clogging. Fig. 12 shows the results of the semi-empirical approach applied to the southbound tunnel and other projects reported in the literature (Tokgöz 2016, Avunduk and Copur 2018, 2019). The consistency I_c and plastic index I_p for the specimen taken from the silty clay along the tunnel alignment of the southbound tunnel are 0.65 and 13.8% respectively, which also substantiates the specimen of clogging material with predominantly strong

clogging potential. Fig. 13 shows the performance of the anomaly detectors applied to the southbound tunnel mapped to the transformed space.

The results from the advance rate detector indicate that four outliers present at distances of 108 m, 109 m, 155 m and 156 m respectively and are spread over the lower area in the feature space in Fig. 13(a). There are five outliers present from the results based upon the cutterwheel torque detector, namely 102 m, 103 m, 109 m, 186 m and 187 m respectively. Except the outlier at 109 m, the rest are also spread over the lower area in the feature space in Fig. 13(b). Both the detectors identify a common outlier at 109 m.

4.2 Discussion

All of the TPs and TNs are spread over the upper and lower areas respectively in the feature space for the first three classifiers, while for the last classifier they are spread the other way around (Fig. 10). This is to say that the coarse sand and the fine sand are classed in accordance with the value of T_t. The coarse sands can be correctly classed when $T_t < 0.5$ (1510 kN and 2983 kN·m) for the first two classifiers and when $T_t < 0.69$ (74 mm/min) for the third classifier as well as when $T_t > 0.38$ (9.8 rpm) for the last classifier. According to Cheng *et al.* (2017), the contact between the cutterwheel and the soil at the tunnel face changes from 'full' contact for tunnelling in fine sand to 'point' contact for tunnelling in coarse sand. This makes the thrust force and T_t lower than those subjected to tunnelling in the fine sand in Fig. 10(a). Further, according to the authors' observations, the EPB shield advances faster in the fine sand than the coarse sand, while tunnelling in the fine sand causes some difficulty in spoil transport, making the screw conveyor rotational speed slower than the coarse sand in Figs. 10(c) and (d). Moreover, tunnelling in the fine sand causes the cutterwheel torque constantly high. Tunnelling in the coarse sand, however, makes the cutterwheel torque to fluctuate significantly, constructing two decision boundaries in the feature space in Fig. 10(b). The cutterwheel torque classifier constructs one major decision boundary at T_t = 0.62-0.82 (3431-4146 kN·m) and R_t = 0.32-0.58 (-298-330 kN·m) and the other at at T_t = 0-0.5 (0-2983 kN·m). The main cause to promote the construction of the two decision boundaries is due to the fact that the change in cutterwheel torque from 2000 kN·m to 4000 kN·m at 95 m distance enforces the cutterwheel torque classifier to construct the other boundary to pursue higher classification accuracy.

Notwithstanding that, the fine sands at distances of 376-405 m and 530-630 m are erroneously classed as the coarse sands towards causing FN = 62 (see Table 6). These results are considered as the main cause to lead to the highest FAR = 35.6%. The discovery rate (DR) and the false alarm rate (FAR) are tabulated in Table 7. Most of the coarse sands are correctly classed for the southbound tunnel, with DR averaging 89.5%. The thrust force classifier provides the highest DR = 93.9% resulting from FP = 15 present at 351-373.5 m distance where the EPB shield penetrates into the fine sand from the coarse sand. Further, a majority of the fine sands are correctly identified and DR is averaged 80.5%. The highest DR = 90.2%, induced by FN = 17 at 493.5-528 m, is given by the screw conveyor rotational speed classifier. The formation of FNs is due to the fact that the mechanical forces, exerted while tunnelling in the fine sand, aggravates the cutterwheel torque and the shield operator attempts to maintain the performance by introducing the rotational speed similar to tunnelling in the coarse sand.

Unlike the southbound tunnel, all of the TPs and TNs are arbitrarily spread over the feature space for the northbound tunnel, meaning that the soils are not classed by T_t or R_t (Fig. 11). Nearly all of the coarse sands are correctly classed, with an average DR = 96.8%. The thrust force classifier gives the highest DR = 100% because it classes all the soils as the coarse sands. This classifier, therefore, fails to class the fine sands, causing FN = 140 in Fig. 11(a). Only one-third of the fine sands are appropriately identified, with an average DR = 31.4% which is far below the performance at the southbound tunnel. The highest DR = 60.7% resulting from FN = 55 present at distances with the fine sand is given by the cutterwheel torque classifier in Fig. 11(b). The main cause to lead to such a great number of misclassifications (i.e., very low DR) present at the northbound tunnel is most likely because the fine sands are spread over a narrow range of 294-502.5 m distance leading to an inability for the proposed classifiers to accentuate patterns in the data to class the fine sands. As a result, the discriminability for determining the decision boundaries at the northbound tunnel against the four classifiers is not as good as the southbound tunnel. On the whole, considering the classification performance, the thrust force classifier is, therefore, considered most effective in identifying the coarse sand, and the screw conveyor rotational speed is deemed most sensitive to tunnelling in the fine sand.

Free water from groundwater inflow and water contained in the soil conditioning agent plays an leading role in clogging potential during tunnel excavation, and tunnelling in clayey soils with 'soft' consistency is deemed high-risk for the development of clogging. Clayey soils due to the availability of free water are likely to be transformed into sticky material. Clogging happens throughout process from excavation at the tunnel face (i.e., primary clogging) up to separation and transport for disposal (i.e., secondary clogging). When clogging occurs, there is a substantial reduction in advance rate and there are also negative impacts upon the cutterwheel torque because of the mechanical forces arising from the excavation-transport-disposal process. In this work, the EPB shield confronts the mixed ground conditions at distances of 108-300 m of the southbound tunnel where the silty clay and the medium sand are present first, followed by the silty clay and the gravelly sand. Hollmann and Thewes (2013) examined 150 samples of 'sticky' material obtained from open shield tunnelling projects. The samples varied between very soft (23% of samples; I_c = 0.4-0.5), soft-medium (58%; I_c = 0.5-0.75) and stiff (19%; I_c = 0.75-1.0) consistency. I_c = 0.65 from the silty clay present at the southbound tunnel shows good agreement with those documented by Hollmann and Thewes (2013). It can be seen from Fig. 13(a) that the first two outliers at distances of 108 m and 109 m identified using the advance rate detector are featured with T_t = 0 and R_t = 0.32, induced by a very low advance rate reaching the lower limit of 30 mm/min. The third outlier at 155 m distance is formed due to T_t = 0.35 and R_t = 0, induced by

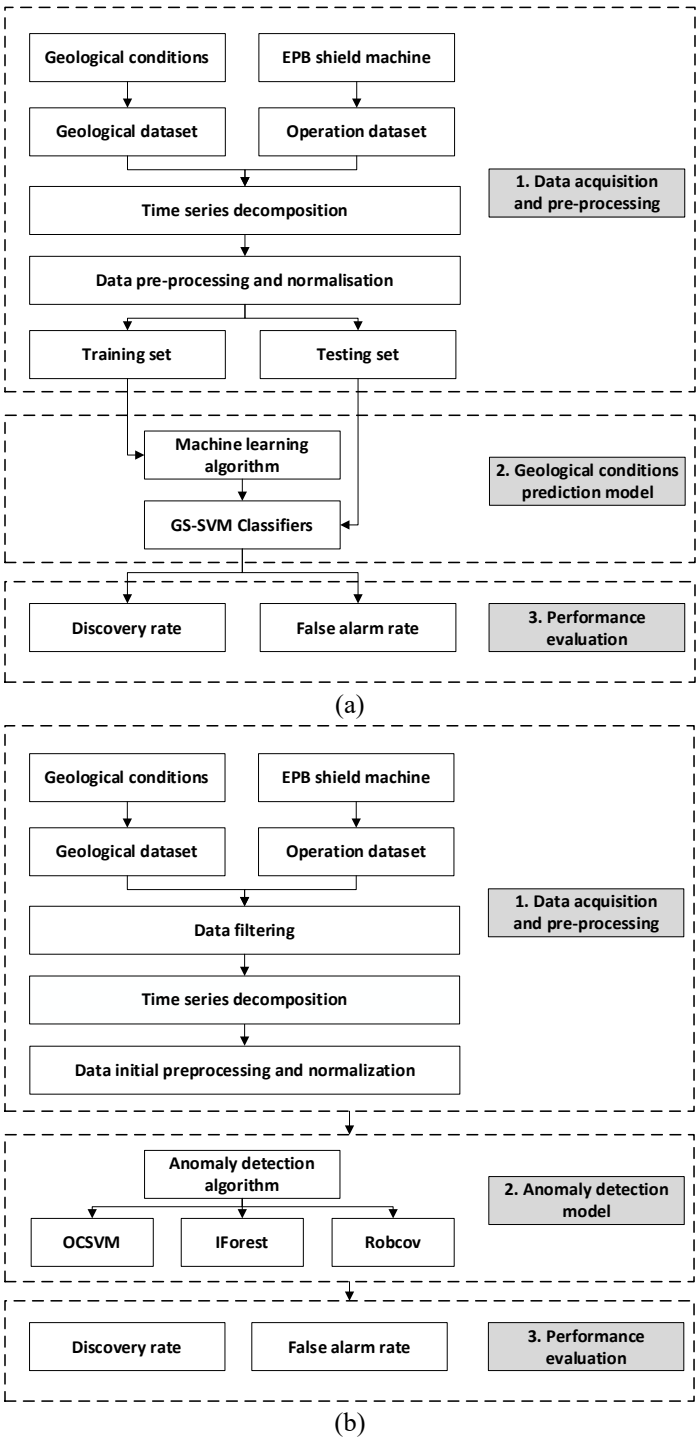

Fig. 14 Flowchart of the machine learning: (a) geological conditions prediction and (b) anomaly detection

an increase in the advance rate to 50 mm/min from 34 mm/min at 154 m distance. The higher advance rate of 50 mm/min from 154 m distance increases T_t and this, in turn, lowers R_t to 0. The last outlier at 156 m distance is formed as a result of $T_t = 0.35$ and $R_t = 1$ resulting from an decline in the advance rate to 50 mm/min from 70 mm/min at 157 m distance. Further, the first outlier at 109 m identified using the cutterwheel torque detector is featured with $T_t = 1$ and $R_t = 0.49$, induced by a very high cutterwheel torque hitting the upper limit of 4300 kN·m in Fig. 13(b). The second outlier at 102 m distance can be characterised by $T_t = 0.33$ and $R_t = 1$ resulting from a decline in the cutterwheel torque to 2800 kN·m from 4100 kN·m at 103 m distance. The third outlier at 103 m distance is formed by $T_t = 0.33$ and $R_t = 0$, caused by an increase in the torque to 4000 kN·m from 2800 kN·m at 105 m distance. The last two outliers at 186 m and 187 m distances can be characterised by $T_t \approx 0$ and $R_t = 0.3$ inducing by an increase in the torque to 4000 kN·m from 3200 kN·m at 185 m distance and $T_t \approx 0$ and $R_t = 0.53$ resulting from a low torque of 3400 kN·m respectively. To summarise, tunnelling in the silty clay with soft consistency lowers the advance rate and lifts up the

cutterwheel torque. The two outliers at 109 m distance of the southbound tunnel are identified by the advance rate and cutterwheel torque detectors respectively. These results are in line with the authors' observations and clearly reflect the negative impacts arising from the development of clogging when tunnelling in such ground containing the sticky material.

Two flowcharts applied to the geological condition prediction and anomaly detection during tunnel construction are presented in Fig. 14. Three main parts are integrated in the flowcharts, namely data acquisition and pre-processing, development of geological classifier and anomaly detector using machine learning algorithms, and performance evaluation. Generally, modern tunnel boring machines are mainly responsible for data acquisition, followed by data pre-processing. The data pre-processing includes time series decomposition, feature selection, and data scaling. Despite that, the optimisation of hyperparameters is deemed necessary before the performance evaluation using the cross-validation accuracy. It is noteworthy that special attention is required when tunnelling proceeds within clay soils of high consistency since the development of clogging can easily be initiated. In light of this, in addition to the above procedures, data filtering to remove data related to tunnelling in soils of low clogging potential is considered as a must-do task prior to data decomposition. Since the validity is verified via an application to the tunnelling project, the proposed flowcharts can therefore be applied to other projects of different geological conditions.

5. Conclusions

This paper has explored the feasibility to identify the change in geological conditions during the shield tunnel constructions at Xi'an Metro line 4 using the machine learning-based data driven approach and examined the potential for the use of anomaly detector to assess the development of clogging. Based upon the results and discussion, some main conclusions can be drawn as follows:

- Most of the coarse sands at the southbound tunnel are correctly classed, with the discovery rate of up to 93.9%. The thrust force classifier is considered most effective in identifying the coarse sand. A majority of the fine sands at the same tunnel are also correctly identified, with the best discovery rate being 90.2%. The screw conveyor rotational speed classifier is most sensitive to tunnelling in the fine sand. However, only one-third of the fine sands at the northbound tunnel are appropriately identified. The fine sands spread over a narrow range significantly lowers the discriminability of the proposed classifiers for determining the decision boundaries at the northbound tunnel.
- Tunnelling in the silty clay with soft consistency at the southbound tunnel lowers the advance rate and lifts up the cutterwheel torque and is deemed high-risk for the development of clayey clogging. The two outliers at 109 m distance of the southbound tunnel are identified using the advance rate and cutterwheel torque detectors, respectively. These results verify the applicability of the proposed anomaly detectors.
- The machine learning-based classifiers and the anomaly detectors proposed in this work are considered effective in identifying the change in geological conditions and detecting the development of clogging during the shield tunnel constructions at Xi'an Metro line 4. Future works to deepen the ability to accentuate patterns in the data to identify more complex changes in geology are needed in order to widen the application horizon of the machine learning-based approaches.

Acknowledgments

This study would not have been possible without financial supports from the Special fund for Basic Scientific Research of Central Colleges, Chang'an University, under Grant No. 300102269502.

References

Basmenj, A.K., Ghafoori, M., Cheshomi, A. and Azandariani, Y.K. (2016), "Adhesion of clay to metal surface; Normal and tangential measurementy", *Geomech. Eng.*, **10**(2), 125-135. https://doi.org/10.12989/gae.2016.10.2.125.

Breiman, L. (2001), "Random forests", *Mach. Learn.*, **45**(1), 5-32.

Cheng, W.C., Ni, J.C., Arulrajah, A. and Huang, H.W. (2018), "A simple approach for characterising tunnel bore conditions based upon pipe-jacking data", *Tunn. Undergr. Sp. Tech.*, **71**, 494-504. https://doi.org/10.1016/j.tust.2017.10.002.

Cheng, W.C., Ni, J.C., Shen, S.L. and Huang, H.W. (2017), "Investigation into factors affecting jacking force: A case study", *P. I. Civ. Eng. Geotec.*, **170**(4), 322-334. https://doi.org/10.1680/jgeen.16.00117.

Cheng, W.C., Wang, L., Xue, Z.F., Ni, J.C., Rahman M. and Arulrajah, A. (2019a), "Lubrication performance of pipejacking in alluvial deposits", *Tunn. Undergr. Sp. Tech.*, **91**, 102991. https://doi.org/10.1016/j.tust.2019.102991.

Cheng, W.C., Ni, J.C., Huang, H.W. and Shen, J.S. (2019b), "The use of tunnelling parameters and spoil characteristics to assess soil types: A case study from alluvial deposits at a pipejacking project site", *B. Eng. Geol. Environ.*, **78**(4), 2933-2942. https://doi.org/10.1007/s10064-018-1288-4.

Cheng, W.C., Bai, X.D., Sheil, B.B., Li, G. and Wang, F. (2020a), "Identifying characteristics of pipejacking parameters to assess geological conditions using optimisation algorithm-based support vector machines", *Tunn. Undergr. Sp. Tech.*, **106**, 103592. https://doi.org/10.1016/j.tust.2020.103592.

Cheng, W.C., Li, G., Ong, D.E.L., Chen, S.L. and Ni, J.C. (2020b), "Modelling liner forces response to very close-proximity tunnelling in soft alluvial deposits", *Tunn. Undergr. Sp. Tech.*, **103**, 103455. https://doi.org/10.1016/j.tust.2020.103455.

Cheng, W.C., Li, G., Liu, N., Xu, J. and Horpibulsuk, S. (2020c), "Recent massive incidents for subway construction in soft alluvial deposits of Taiwan: A review", *Tunn. Undergr. Sp. Tech.*, **96**, 103178. https://doi.org/10.1016/j.tust.2019.103178.

Cleveland, R.B., Cleveland, W.S., McRae, J.E. and Terpenning, I.J. (1990), "STL: A seasonal-trend decomposition procedure based on loess", *J. Off. Stat.*, **6**(1), 3-33.

Eskandari, F., Goharrizi, K.G. and Hooti, R. (2018), "The impact of EPB pressure on surface settlement and face displacement in intersection of triple tunnels at Mashhad metro", *Geomech. Eng.*, **15**(2), 769-774.

https://doi.org/ 10.12989/gae.2018.15.2.769.
Feinendegen, M., Ziegler, M., Weh, M. and Spagnoli, G. (2011), "Clogging during EPB-tunnelling: Occurrence, classification and new manipulation methods", *Proceedings of the ITA-AITES World Tunnel Congress*, Helsinki, Finland, January.
Fountaine, E.R. (1954), "Investigations into the mechanism of soil adhesion", *Eur. J. Soil Sci.*, **5**(2), 251-263. https://doi.org/10.1111/j.1365-2389.1954.tb02191.x.
Friedman, J.H. (1991), "Multivariate adaptive regression splines", *Ann. Stat.*, **19**, 1-67.
Gao, W. and He, T.Y. (2017), "Displacement prediction in geotechnical engineering based on evolutionary neural network", *Geomech. Eng.*, **13**(5), 845-860. https://doi.org/10.12989/gae.2017.13.5.845.
Goh, A.T.C. and Hefney, A.M. (2010), "Reliability assessment of EPB tunnel-related settlement", *Geomech. Eng.*, **2**(1), 57-69. https://doi.org/10.12989/gae.2010.2.1.057.
Hollmann, F.S. and Thewes, M. (2013), "Assessment method for clay clogging and disintegration of fines in mechanised tunnelling", *Tunn. Undergr. Sp. Tech.*, **37**, 96-106. https://doi.org/10.1016/j.tust.2013.03.010.
Javadi, A.A. and Rezania, M. (2009), "Applications of artificial intelligence and data mining techniques in soil modeling", *Geomech. Eng.*, **1**(1), 53-74. https://doi.org/10.12989/gae.2009.1.1.053.
Lee, C.J., Jeon, Y.J. Kim, S.H. and Park, I.J. (2016), "The influence of tunnelling on the behaviour of pre-existing piled foundations in weathered soil", *Geomech. Eng.*, **11**(4), 553-570. https://doi.org/10.12989/gae.2016.11.4.553.
Li, S., Liu, B., Nie, L., Liu, Z., Tian, M., Wang, S., Su, M. and Guo, Q. (2015), "Detecting and monitoring of water inrush in tunnels and coal mines using direct current resistivity method: A review", *J. Rock Mech. Geotech. Eng.*, **7**(4), 469-478. https://doi.org/10.1016/j.jrmge.2015.06.004.
Li, S., Nie, L. and Liu, B. (2018b), "The practice of forward prospecting of adverse geology applied to hard rock TBM tunnel construction: The case of the Songhua River water conveyance project in the middle of Jilin Province", *Engineering*, **4**(1), 131-137. https://doi.org/10.1016/j.eng.2017.12.010.
Li, S., Xu, S., Nie, L., Liu, B., Liu, R., Zhang, Q., Zhao, Y., Liu, Q., Wang, H., Liu, H. and Guo, Q. (2018a), "Assessment of electrical resistivity imaging for pre-tunneling geological characterization – a case study of the Qingdao R3 metro line tunnel", *J. Appl. Geophys.*, **153**, 38-46. https://doi.org/10.1016/j.jappgeo.2018.03.024.
Liu, B., Liu, Z., Li, S., Fan, K., Nie, L. and Zhang, X. (2017a), "An improved time-lapse resistivity tomography to monitor and estimate the impact on the groundwater system induced by tunnel excavation", *Tunn. Undergr. Sp. Tech.*, **66**, 107-120. https://doi.org/10.1016/j.tust.2017.04.008.
Liu, B., Liu, Z., Nie, L., Su, M., Sun, H., Fan, K., Zhang, X. and Pang, Y. (2017b), "Comprehensive surface geophysical investigation of karst caves ahead of the tunnel face: A case study in the Xiaoheyan section of the water supply project from Songhua River, Jilin, China", *J. Appl. Geophys.*, **144**, 37-49. https://doi.org/10.1016/j.jappgeo.2017.06.013.
Liu, J.K., Luan, H.J., Zhang, Y.C., Sakaguchi, O. and Jiang, Y.J. (2020), "Prediction of unconfined compressive strength ahead of tunnel face using measurement-while-drilling data based on hybrid genetic algorithm", *Geomech. Eng.*, **22**(1), 81-95. https://doi.org/10.12989/gae.2020.22.1.081.
Luat, N.V., Lee, K. and Thai, D.K. (2020a), "An evolutionary hybrid optimization of MARS model in predicting settlement of shallow foundations on sandy soils", *Geomech. Eng.*, **21**(6), 583-598. https://doi.org/ 10.12989/gae.2020.21.6.583.
Luat, N.V., Nguyen, V.Q. and Lee, S. (2020b), "Application of artificial neural networks in settlement prediction of shallow foundations on sandy soils", *Geomech. Eng.*, **20**(5), 385-397. https://doi.org/10.12989/gae.2020.20.5.385.
Mazek, S.A. (2014), "Evaluation of surface displacement equation due to tunnelling in cohesionless soil", *Geomech. Eng.*, **7**(1), 55-73. https://doi.org/10.12989/gae.2014.7.1.055.
O'Dwyer, K.G., McCabe, B.A. and Sheil, B.B. (2019), "Interpretation of pipe-jacking and lubrication records for drives in silty soil", *Undergr. Sp.*, **5**(3), 199-209. https://doi.org/10.1016/j.undsp.2019.04.001.
Park, T.W., Kim, H.G., Tanvirn, M.T., lee, J.B. and Moon, S.J. (2018), "Influence of coarse particles on the physical properties and quick undrained shear strength of fine-grained soils", *Geomech. Eng.*, **14**(1), 99-105. https://doi.org/10.12989/gae.2018.14.1.099.
Persons, W.M. (1919), *Indices of Business Conditions: An Index of General Business Conditions*, Harvard University Press.
Rezaei, A.H., Shirzehhagh, M. and Golpasand, M.R.B. (2019), "EPB tunneling in cohesionless soils: A study on Tabriz Metro settlements", *Geomech. Eng.*, **19**(2), 153-165. https://doi.org/ 10.12989/gae.2019.19.2.153.
Schölkopf, B., Platt, J.C., Shawe-Taylor, J., Smola, A.J. and Williamson, R.C. (2001), "Estimating the support of a high-dimensional distribution", *Neural Comput.*, **13**(7), 1443-1471. https://doi.org/10.1162/089976601750264965.
Sheil, B.B., Curran, B.G. and McCabe, B.A. (2016), "Experiences of utility microtunnelling in Irish limestone, mudstone and sandstone rock", *Tunn. Undergr. Sp. Tech.*, **51**, 326-337. https://doi.org/10.1016/j.tust.2015.10.019.
Sheil, B.B., Suryasentana, S.K. and Cheng, W.C. (2020), "Assessment of anomaly detection methods applied to microtunneling", *J. Geotech. Geoenviron. Eng.*, **146**(9). https://doi.org/10.1061/(ASCE)GT.1943-5606.0002326.
Spagnoli, G., Feinendegen, M., Stanjek, H. and Azzam, R. (2011a), "Soil conditioning for clays in EPBMs", *Tunn. Tunn. Int.*, **43**(10), 56-61.
Spagnoli, G., Klitzsch, N., Fernandez-Steeger, T., Feinendegen, M., Rey, A.R., Stanjek, H. and Azzam, R. (2011b), "Application of electro-osmosis to reduce the adhesion of clay during mechanical tunnel driving", *Environ. Eng. Geosci.*, **17**(4), 417-426. https://doi.org/10.2113/gseegeosci.17.4.417.
Thewes, M. (1999), "Adhesion of clay soil in tunnel drives with slurry shields (In German: Adhäsion von Tonböden beim Tunnelvortrieb mit Flüssigkeitsschilden)", Berichte aus Bodenmechanik und Grundbau der Bergischen Universität Wuppertal, Fachbereich Bauingenieurwesen, Bd. 21. Shaker Verlag, Aachen, Germany.
Thewes, M. and Hollmann, F.S. (2014), "TBM-specific testing scheme to assess the clogging tendency of rock", *Geomech. Tunn.*, **7**(5), 520-527. https://doi.org/10.1002/geot.201400048.
Thewes, M. and Hollmann, F.S. (2016), "Assessment of clay soils and clay-rich rock for clogging of TBMs", *Tunn. Undergr. Sp. Tech.*, **57**, 122-128. https://doi.org/10.1016/j.tust.2016.01.010.
Wang, Z.F., Cheng, W.C. and Wang, Y.Q. (2018), "Investigation into geohazards during urbanization process of Xi'an, China", *Nat. Hazards*, **92**(3), 1937-1953. https://doi.org/10.1007/s11069-018-3280-5.
Xu, J.C., Ren, Q.W. and Shen, Z.H. (2017), "Sensitivity analysis of the influencing factors of slope stability based on LS-SVM", *Geomech. Eng.*, **13**(3), 447-458. https://doi.org/10.12989/gae.2017.13.4.447.
Zhang, W.G. and Goh, A.T.C. (2016), "Evaluating seismic liquefaction potential using multivariate adaptive regression splines and logistic regression", *Geomech. Eng.*, **10**(3), 269-284. https://doi.org/10.12989/gae.2016.10.3.269.
Zhang, W.G., Zhang, R.H. and Goh, A.T.C. (2018), "MARS inverse analysis of soil and wall properties for braced

excavations in clays", *Geomech*. *Eng*., **16**(6), 577-588.
https://doi.org/ 10.12989/gae.2018.16.6.577.

IC